



## Article

# Impacts of the All-Sky Assimilation of FY-3C and FY-3D MWHS-2 Radiances on Analyses and Forecasts of Typhoon Hagupit

Keyi Chen <sup>1,\*</sup> , Zhenxuan Chen <sup>1</sup>, Zhipeng Xian <sup>2,3</sup> and Guancheng Li <sup>4</sup><sup>1</sup> School of the Atmospheric Sciences, Chengdu University of Information Technology, Chengdu 610225, China<sup>2</sup> International Center for Climate and Environment Sciences, Institute of Atmospheric Physics, Chinese Academy of Sciences, Beijing 100029, China<sup>3</sup> University of Chinese Academy of Sciences, Beijing 100049, China<sup>4</sup> Eco-Environmental Monitoring and Research Center, Pearl River Valley and South China Sea Ecology and Environment, Guangzhou 510611, China

\* Correspondence: cky@cuit.edu.cn

**Abstract:** With the Microwave Humidity Sounder-2 (MWHS-2)/Fengyun (FY)-3D in operation, this is the first study to evaluate the impact of a joint assimilation of MWHS-2 radiances under all-sky conditions from both the FY-3C and FY-3D satellites on typhoon forecasting within regional areas. In this study, Typhoon Hagupit in 2020 was chosen to investigate the impacts of assimilating MWHS-2 radiances; the forecasting performances of the joint assimilation method were slightly better than the experiments assimilating MWHS-2 observations from FY-3C or FY-3D only, and the results of the latter two experiments were comparable, especially in terms of the landfall location of Hagupit. With additional assimilated cloud- and precipitation-affected MWHS-2 observations, improved typhoon track and intensity forecasts as well as forecasts of the precipitation caused by Hagupit were achieved due to the improved analyses of relative humidity, temperature and wind fields around Hagupit compared to the clear-sky assimilation experiments. In addition, the channel-selection scheme evidently affected the forecasting performance; that is, the radiances from the MWHS-2 118 GHz and 183 GHz channels provided opposite results in terms of the Hagupit track, and this finding needs further investigation in the future.



**Citation:** Chen, K.; Chen, Z.; Xian, Z.; Li, G. Impacts of the All-Sky Assimilation of FY-3C and FY-3D MWHS-2 Radiances on Analyses and Forecasts of Typhoon Hagupit. *Remote Sens.* **2023**, *15*, 2279. <https://doi.org/10.3390/rs15092279>

Academic Editor: Yuriy Kuleshov

Received: 31 March 2023

Revised: 17 April 2023

Accepted: 17 April 2023

Published: 26 April 2023



**Copyright:** © 2023 by the authors. Licensee MDPI, Basel, Switzerland. This article is an open access article distributed under the terms and conditions of the Creative Commons Attribution (CC BY) license (<https://creativecommons.org/licenses/by/4.0/>).

**Keywords:** all-sky assimilation; typhoon forecasts; Fengyun satellites; microwave humidity sounders

## 1. Introduction

The statistics of European Centre for Medium-Range Weather Forecasts (ECMWF) show that satellite data provide over 90% of the assimilated data in global numerical weather prediction (NWP) systems, while approximately 75% of the satellite data are removed after a strict quality control process due to cloud and precipitation effects or overly complex underlying surfaces [1,2]. However, an average of 70% of the globe is covered by clouds [3], which are meteorologically sensitive [4]. If the initial fields in these areas are not sufficiently accurate, the regional forecasting errors will greatly increase [5]. Therefore, the all-sky assimilation approach was proposed by Geer and Bauer [6]; this approach involves assigning observation errors that vary as a function of the cloud coverage to the radiance and was first applied to microwave observations. For microwave sounders, the temperature or humidity sounding channels are sensitive to the cloud liquid water content [7], meaning that many observations cannot be assimilated under clear conditions. With all-sky assimilation, the impacts of microwave observations on NWP can be greatly improved due to the increasing number of microwave instruments used and the efficient use of cloud-affected radiances. Such observations are widely assimilated to adjust initial moisture fields [8] because of their better detection abilities in the presence of clouds [9]. Therefore, more

accurate cloud and precipitation initialization conditions can be obtained [10], and cloud and precipitation modeling can be improved [11,12]. At present, an increasing number of NWP operational centers around the world have used or are developing all-sky microwave assimilation algorithms [9,13–16]. Studies have demonstrated that all-sky satellite data assimilation methods can improve relatively short-range tropical cyclone forecasts [17]. All-sky microwave (MW) observing data assimilations can improve the tropospheric wind fields in the JMA global NWP system, leading to improved typhoon-track predictions [17]. Further research on AMSU-A operational all-sky assimilations at ECMWF has demonstrated that such assimilations can aid in typhoon forecasting by providing additional mid-level information near typhoon cores [18].

For the regional NWP system, there are also some remarkable impacts of satellite radiance assimilations in typhoon forecasts, especially under all-sky conditions. The HWRF (Hurricane WRF) and WRF (ARW) models show wide application potentials in typhoon NWP research development, and these two models have different dynamic cores [19]. The HWRF model has specific physical parameterization schemes and uses an advanced vortex initialization. However, numerous studies have focused on assimilating atmospheric motion vectors [20–24], infrared observations [25] or MW observations [26] into the HWRF model. All these methods showed some positive impacts on the resulting typhoon predictions. As a result, such methods can be further applied in future studies. On the other hand, the WRF (ARW) model is portable on parallel computing platforms [27] and can be more efficient than the HWRF model. Regional NWP systems are more mature than other systems due to the large number of similar studies involving WRF (ARW) modeling. This method can provide more information on the vertical profiles and inner structures of typhoons by assimilating AMSU-A radiances with WRFDA data [28] and can also produce better depictions of track forecasts [28–31]. MHS data have also been confirmed to provide heightened improvements in mid-level moisture predictions and in intensity forecasts [32]. In addition, assimilating AMSU-A, AMSU-B and MHS radiances can also be beneficial for improving typhoon intensity forecasts with EAKF [33]. With the successful launch of the Chinese Fengyun-3C (FY-3C) satellite, the Microwave Humidity Sounder II (MWHS-2) observations are expected to play a more important role in assimilation systems, as these observations can effectively improve the quality of the initial conditions [34]. The observations of the MWHS-2 instrument onboard FY-3C exhibit an overall good data quality that is comparable to other similar instruments [35], and these observations have been operationally used in ECMWF since April 2016. In the ECMWF global model, assimilating FY-3C/MWHS-2 data could introduce some improvement to the accuracy of the 12 h forecasts and 2–4 day wind forecasts [36]. In the Met Office global model, MWHS-2 was found to reduce the 24 h forecast error significantly, by 0.6% [37]. With regional models, assimilating FY-3C/MWHS-2 observations under both clear- and all-sky conditions improved the forecasts of typhoons [38], Meiyu [39] and the Southwest Vortex [40]. Later, FY-3D was successfully launched in October 2017. The MWHS-2 instruments onboard FY-3C and FY-3D are identical, but the first departures are reduced as a result of the different calibration methods applied in FY3D/MWHS-2 [41], introducing a small but significant improvement for low-level humidity forecasts [42]. Therefore, FY-3D/MWHS-2 observations were put into operational use by the ECMWF in December 2019 [43], thereby further enhancing the positive impact of the FY-3 sensors [44].

Since both FY-3C/MWHS-2 and FY-3D/MWHS-2 have been fully accessed and made operational for ECMWF and other weather centers by assimilating globally conventional data and many other types of observations, the independent and combined impacts of FY-3C/MWHS-2 and FY-3D/MWHS-2, excluding the state-of-the-art and 118 GHz and 183 GHz channel sensitivity, are also of interest in regional forecasts depicting high-impact weather processes for the purpose of research configurations. Because not all regional weather centers can obtain diversified observations and because the officially delivered Fengyun satellite data may be the only dense observation source compared to the sparse conventional data, especially in some underdeveloped areas, the purpose of this study

is to further understand the independent and combined impacts of FY-3C/D/MWHS-2 radiances in the assimilations and forecasts of the regional NWP considering their different descending and ascending orbits and starting with typhoon cases. In the rest of this paper, an overview of the observations, model configuration and methodology is presented in Section 2, followed by the experimental settings in Section 3. In Section 4, we analyze the impacts of assimilating MWHS-2 radiances in different experiments. Conclusions and discussions are given in Section 5.

## 2. MWHS-2 Observations, Model Configuration and Methodology

### 2.1. MWHS-2 Observations

FY-3C is a morning polar-orbiting satellite with an equatorial cross time (ECT) of 10:15 (descending) launched in September 2013, and FY-3D is an afternoon orbiting satellite with an ascending ECT of 13:29 launched in November 2017. The MWHS-2 instruments onboard both satellites are second-generation microwave humidity sounders, and the detailed parameters of their 15 channels are listed in Table 1. Two window channels at 89 and 150 GHz are used to detect background microwave radiation and precipitation and to retrieve surface emissivity; five channels at the 183 GHz water vapor absorption line provide the vertical humidity information of the atmosphere for the NWP; eight channels sampling the 118 GHz atmospheric oxygen absorption line are primarily sensitive to atmospheric temperature; and the lowest peaking 118 GHz channel (channel 7) is also sensitive to low-level humidity due to the water vapor continuum.

**Table 1.** Characteristics of Microwave Humidity Sounder-2 Channels.

Channel Number	Central Frequency (GHz) and Polarization	FOV	Swath Width (km)	Peak Height (hPa)	Horizontal Resolution (km)
1	89.0 (V)	98	2660	/	29
2	118.75 ± 0.08 (H)			20	29
3	118.75 ± 0.2 (H)			60	29
4	118.75 ± 0.3 (H)			100	29
5	118.75 ± 0.8 (H)			250	29
6	118.75 ± 1.1 (H)			300	29
7	118.75 ± 2.5 (H)			700	29
8	118.75 ± 3.0 (H)			/	29
9	118.75 ± 5.0 (H)			/	29
10	150.0 (V)	98	2660	/	16
11	183.31 ± 1 (H)			350	16
12	183.31 ± 1.8 (H)			400	16
13	183.31 ± 3 (H)			500	16
14	183.31 ± 4.5 (H)			550	16
15	183.31 ± 7 (H)			650	16

In addition, because of the absorption and emission of liquid water and the scattering of ice and precipitation, the 118 GHz band is also sensitive to clouds and precipitation [45]. Notably, 118 GHz channels are flown on FY-3C for the first time globally and have played an important role in all-sky assimilation for NWP since the satellite was activated [36]. Due to their smaller global biases in most channels (except channel 15) due to the different calibration methods, FY-3D/MWHS-2 observations show comparable or even better data quality than FY-3C/MWHS-2 observations [41].

### 2.2. Model Configurations

All experiments performed in this study were conducted by using the Weather Research and Forecasting Model (WRF) (v 3.9.1.1) and the three-dimensional variational component of the WRFDA system [46] developed by the National Center for Atmospheric Research (NCAR). This method can provide an optimal analysis of the atmospheric state through the iterative minimization of a prescribed cost function as follows:

$$J(\mathbf{x}) = \frac{1}{2}(\mathbf{x} - \mathbf{x}_b)^T \mathbf{B}^{-1}(\mathbf{x} - \mathbf{x}_b) + \frac{1}{2}(\mathbf{y} - H(\mathbf{x}))^T \mathbf{R}^{(-1)}(\mathbf{y} - H(\mathbf{x})) \quad (1)$$

where  $x$  represents the analysis field,  $x_b$  represents the background field,  $B$  represents the N-dimensional background error covariance matrices (where N is the degrees of freedom of the background field),  $y$  represents the observation field,  $H$  is the nonlinear observation operator (used to map the model variable into the observation space) and  $R$  represents the M-dimensional observation error covariance matrices (where M is the degrees of freedom of the observation field).

The default control variables (CV option five), including the stream function, unbalanced velocity potential, unbalanced temperature, unbalanced surface pressure and pseudo-relative humidity, were adopted in the experiments performed in this study. The National Meteorological Center (NMC) method [47] was applied to provide the case-dependent background error covariance matrices by calculating the difference in the 24 and 12 h forecasts initiated from NCEP Global Data Assimilation System (GDAS)/final (FNL) 0.25° Global Tropospheric Analyses Grids at 0000 and 1200 UTC (<https://rda.ucar.edu/datasets/ds083.3/#!description>, accessed on 21 September 2021) for each day of the previous month in each case. Since no FY-3 microwave humidity sounding data were contained in the FNL analysis data ([https://www.emc.ncep.noaa.gov/gmb/STATS/html/model\\_changes.html](https://www.emc.ncep.noaa.gov/gmb/STATS/html/model_changes.html), accessed on 21 September 2021), the results of the assimilating experiments were objective. In addition, the best-track data from the Japan Meteorological Agency (JMA) were used to evaluate the forecasted typhoon track and intensity results.

### 2.3. Dynamic Emissivity Retrieval

Although surface emissivity is a crucial parameter in radiative transfer models, it is difficult to accurately retrieve over land due to the complexity of land types and the large diurnal variations in skin temperature. Different from the Tool to Estimate Land Surface Emissivity at Microwaves and Millimeter waves (TELSEM) atlas [48], which provides monthly average surface emissivity data, the dynamic emissivity retrieved from the window channels (i.e., at 89 GHz and 150 GHz) provides more accurate values closer to the real surface state [49,50]. Chen et al. [50] demonstrated that the 89 GHz channel is more sensitive to middle- and low-latitude surfaces, while the 150 GHz channel is more sensitive to high-latitude surfaces, especially surfaces covered by ice and snow. Therefore, the 89 GHz channel was applied herein for the dynamic emissivity retrieval based on the studied domain under both clear-sky and all-sky conditions.

Assuming that the atmosphere is parallel to a flat, nonscattering plane, given the zenith angle ( $\theta$ ) and frequency ( $\nu$ ), the brightness temperature observed by the satellite sensor can be expressed as follows:

$$T_b = \varepsilon_{(\theta,\nu)} T_s \Gamma_{(\theta,\nu)} + (1 - \varepsilon_{(\theta,\nu)}) T_{(\theta,\nu)}^\downarrow \Gamma_{(\theta,\nu)} + T_{(\theta,\nu)}^\uparrow \quad (2)$$

where  $\varepsilon_{(\theta,\nu)}$  is the surface emissivity,  $T_s$  is the surface skin temperature from the background field,  $T_{(\theta,\nu)}^\downarrow$  and  $T_{(\theta,\nu)}^\uparrow$  are the upwelling and downwelling radiations inverted by the observation operator, respectively, and  $\Gamma_{(\theta,\nu)}$  is the net atmospheric transmissivity. Therefore, the emissivity can be derived by the following equation:

$$\varepsilon_{(\theta,\nu)} = \frac{T_b - \left( T_{(\theta,\nu)}^\uparrow + T_{\theta,\nu}^\downarrow \Gamma_{(\theta,\nu)} \right)}{(T_s - T_{(\theta,\nu)}^\downarrow) \Gamma_{(\theta,\nu)}} \quad (3)$$

Under clear-sky conditions, the results retrieved at 89 GHz were applied when the difference between the emissivity retrieval and its equivalent value from TELSEM was less than 0.2 and greater than 0.5. Under all-sky conditions, the retrieved dynamic surface emissivity was adopted when the emissivity retrieval from the 89 GHz channel was between 0.55 and 1 and the difference between the emissivity retrieval and its equivalent value from TELSEM was less than 0.09. Otherwise, the value from the TELSEM was used as the surface emissivity in the assimilation. As shown in Figure 1, the dynamic emissivity retrieved

from the window channel (at 89 GHz) displayed more variations over land under both clear-sky (Figure 1b) and all-sky (Figure 1c) conditions than the emissivity atlas (Figure 1a), especially over East and South China. Additionally, the strong scattering of thick clouds makes the brightness temperatures lower, leading to unphysically justified depressed emissivity retrievals [51]. When clouds present south of 25°N, dynamic emissivity values larger than 0.9 may not reflect the real surface emissivity under clear-sky conditions (Figure 1b), although this kind of problem was reasonably reduced under all-sky conditions (Figure 1c) owing to the tighter quality control of the emissivity retrievals. The atmospheric initial conditions can potentially be improved with the more realistically detailed dynamic emissivity values retrieved under all-sky conditions.

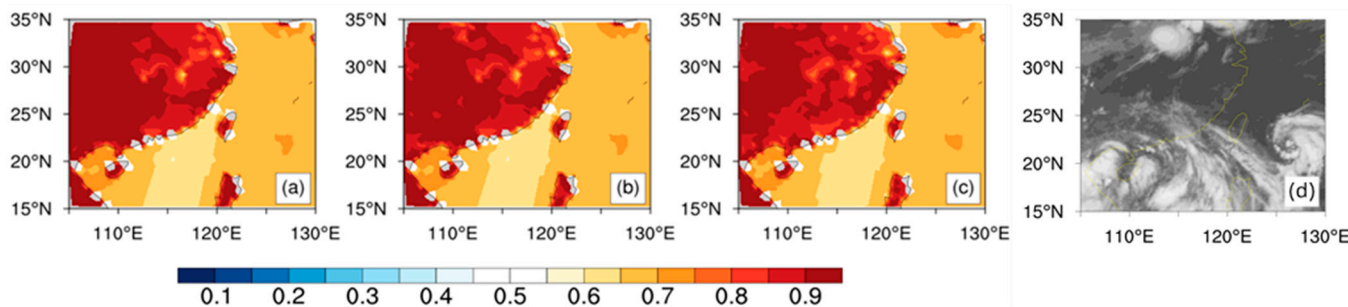


**Figure 1.** The emissivity atlas (a), clear-sky emissivity retrievals (b) and all-sky emissivity retrievals (c) from the FY-3C/MWHS-2 89 GHz channel and the FY-2G satellite black-body temperature product (d) at 1800 UTC on 1 August 2020.

2.4. Observation Errors

Affected by the inaccuracy of the radiative transfer calculation in cloudy and high-precipitation areas and by the poor performances of numerical cloud and precipitation forecasts, the first-guess departures (OMB) show highly non-Gaussian behaviors and thus cannot meet the requirements established in the framework of data assimilation theory. Geer et al. [6,52] proposed an observation model (i.e., the symmetric error model) to assign reasonable observation errors to highly non-Gaussian behaviors of the first-guess departures by applying the RTTOV-SCATT as the observation operator. To measure the cloud amount, the scattering index (SI) [53] is defined in this model as the difference between the brightness temperatures (TBs) at 90 GHz and 150 GHz for the observation and first-guess fields, respectively, based on the different scattering effects of precipitation-sized ice particles on TBs at 90 GHz and 150 GHz. Then, the symmetric cloud predictor can be described as follows:

$$C_{SYM} = \frac{SI_{obs} + SI_{FG}}{2} \tag{4}$$

Therefore, the symmetric observation error can be given as follows:

$$g(C_{SYM}) = \begin{cases} g_{clr} & \in C_{SYM} \leq C_{clr} \\ g_{clr} + (g_{cld} - g_{clr}) \left( \frac{C_{SYM} - C_{clr}}{C_{cld} - C_{clr}} \right)^2 & \in C_{clr} \leq C_{SYM} \leq C_{cld} \\ g_{cld} & \in C_{SYM} \geq C_{cld} \end{cases} \tag{5}$$

where  $g_{clr}$  and  $g_{cld}$  represent the observational errors under clear-sky conditions and all-sky conditions, respectively, and  $C_{clr}$  and  $C_{cld}$  give the ranges over which the main increases in the corresponding observation errors occur. The observation error model for FY-3C/MWHS-2 is basically the same as that developed by Xian et al. [38], and the symmetric error model for FY-3D/MWHS-2 is displayed in Figure 2.

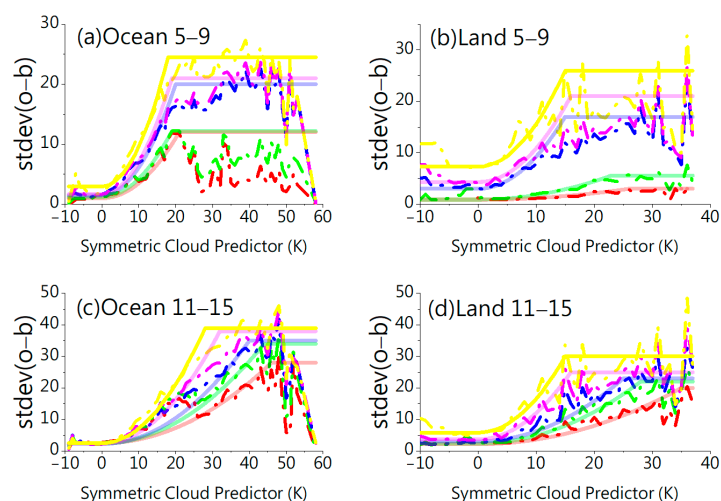


**Figure 2.** The standard deviations in the FY-3D/MWHS-2 first-guess departures (dashed lines) as a function of the symmetric cloud predictors for channels 5–9 (the upper yellow, purple, blue, green, and red lines correspond to channels 5 through 9, respectively) and 11–15 (the lower yellow, purple, blue, green, and red lines correspond to channels 11 through 15, respectively) along with the applied observation errors (solid lines).

For clear-sky assimilations, the cloud liquid water path (CLWP) is calculated to determine whether the observations are affected by clouds and precipitation, and observations with CLWP values greater than 0.2 are considered cloud- and precipitation-affected data and are thus removed. The observation errors assigned to each FY-3D/MWHS-2 channel under clear-sky conditions are shown in Table 2.

**Table 2.** The observation errors assigned to each channel used in FY-3D/MWHS-2 under clear-sky conditions.

Channel	$\sigma_{clr}$	
	Ocean	Land
2	4.9	4.9
3	2.3	2.4
4	1.3	1.5
5	1.0	0.9
6	1.2	0.9
7	1.5	3.0
11	2.5	2.2
12	2.4	2.4
15	2.5	5.8

### 3. Experiment Settings

#### 3.1. Overview of the Typhoon Case

Typhoon Hagupit, which occurred in 2020, was selected to compare the impacts of assimilating MWHS-2 radiance data from FY-3C and FY-3D under clear-sky and all-sky conditions. A tropical depression developing over the Philippine Sea on 30 July 2020 intensified to a tropical storm and was officially named Hagupit by the JMA at 1200 UTC on 1 August, moving northwestward along the edge of the Western Pacific Subtropical High (WPSH). It was upgraded to a strong tropical storm at 2100 UTC on 1 August and quickly strengthened to a severe typhoon at 6 UTC on 3 August with a maximum central wind speed of approximately 42 m/s. With the weakening and extinction of Typhoon Sinlaku, the water vapor transported by the southwestward flow of the summer monsoon to Hagupit was significantly intensified, causing Typhoon Hagupit to develop rapidly, together with the increased sea surface temperatures in the area where Typhoon Hagupit moved. Hagupit made landfall over Yueqing City in Zhejiang Province at 1930 UTC on

3 August with a maximum central wind speed of approximately 38 m/s and a central pressure of approximately 975 hPa. The typhoon then began to weaken and moved northward slowly before dissipating following a brief intensification spanning several days when moving northeastward offshore after passing through Zhejiang and Jiangsu provinces. This severe typhoon caused direct economic losses of CNY 10.46 billion and affected Zhejiang, Fujian, Shanghai and Jiangsu provinces to various extents.

### 3.2. Assimilation Experiment Settings

In this study, seven experiments were carried out to assess the impacts of assimilating FY-3C/MWHS-2 and FY-3D/MWHS-2 radiance data, both individually and cooperatively, using the 3DVAR approach within the WRFDA system on the resulting forecasts of Typhoon Hagupit; the experiments included a control run without any data assimilation (denoted as CON), two clear data-assimilating experiments with FY-3C/MWHS-2 observations (3C-CLEAR) and FY-3D/MWHS-2 observations (3D-CLEAR), two all-sky data-assimilating experiments with the two FY-3 satellite radiances separately (denoted as 3C-ALLSKY and 3D-ALLSKY), and two experiments with FY-3C/MWHS-2 and FY-3D/MWHS-2 data assimilated together under clear-sky (CD-CLEAR) and all-sky (CD-ALLSKY) conditions.

All the experiments started at 1800 UTC on 31 July 2020 and lasted until 0600 UTC on 5 August 2020 with a time step of 60 s and a spin-up time of 18 h. The model configurations include the Lambert projection and  $540 \times 480$  grids with a horizontal resolution of 15 km centered at (25°N, 135°E). The main physical parameterization schemes are listed as follows: the Purdue–Lin [54] microphysics scheme, the Kain–Fritsch [55] cumulus convection scheme, the rapid radiative transfer model scheme [56], the Dudhia [57] scheme, the Yonsei University (YSU) [8] boundary layer scheme, the surface layer scheme based on the fifth-generation Pennsylvania State University–National Center for Atmospheric Research Mesoscale Model (MM5) parameterization [58] and the Noah-Multiparameterization land surface model scheme [59]. For channel selection, the same channel schemes as those selected in ECMWF (i.e., channels 2–6, 11, 12, 15 and 7 over sea are assimilated) are applied here according to the study by Lawrence et al. [36].

To use as many observations as possible in each assimilation window, the analyses were generated every 12 h (i.e., 0000 and 1200 UTC) when assimilating FY-3C/MWHS-2 data only and every 6 h (i.e., 0000, 0600, 1200, 1800 UTC) when assimilating FY-3D/MWHS-2 data only and when assimilating the two FY-3/MWHS-2 observation groups together.

The background conditions applied in the first analysis were obtained from the 18 h forecast initiated from the FNL analysis at 1800 UTC on 31 July 2020. The 6 or 12 h forecasts integrated by the WRF model were used as the background conditions in the following cycle, and the lateral boundaries were updated using the FNL analysis data at 6 or 12 h intervals.

### 3.3. Quality Control and Bias Correction

Before any assimilation began, the large observation errors caused by instruments and other factors had to be removed to ensure the quality of the assimilation processes. A quality control scheme [17,18] was adopted for both the clear-sky and all-sky assimilations, including an extreme value check (to remove the radiance data with TBs lower than 50 K or higher than 550 K), a surface type check (to remove radiance data over mixed surface types), a scanning angle check (to remove the first and last five scan angles in each swath edge) [7], a first-guess departure check (to remove the radiance data if the bias corrected normalized first-guess departure (OMB) exceeded  $3\sigma$ , where  $\sigma$  represents the specified standard deviation of the observation errors), an elevation check (to remove the radiance data over 1500 m for channel 11, 1000 m for channels 12–13, and 800 m for channels 14–15) and a thinning step with a spacing of 60 km. The variational bias correction (VarBC) scheme [60] was utilized to correct the systematic errors between the observed brightness temperatures and the simulated TBs.

Figure 3 displays the probability distribution functions (PDFs) of the absolute and normalized first-guess departures of the MWHS-2 channels 2, 6, 11 and 15 of FY-3C/D along with roughly fitted Gaussians before quality control under all-sky conditions at 0000 UTC on 2 August 2020. As mentioned in Section 2.4, the PDFs of the first-guess departures showed obvious non-Gaussian characteristics during the assimilation of satellite data under all-sky conditions. The observation error model based on the “symmetric error model” could effectively transform the highly non-Gaussian PDFs, making them more similar to a Gaussian distribution. Figure 3 shows that all channels showed different degrees of non-Gaussian behavior before normalization and roughly fitted Gaussian behavior after normalization. The observations and model disagreed in terms of rain and precipitation, leading to large positive or negative first-guess departures. The PDFs of the first-guess departure of channels 5–7, which are sensitive to clouds (Figure 3b,f), and of channels 11–15, which are sensitive to humidity (Figure 3c,d,g,h), were non-Gaussian (e.g., the skewness values of the PDF were  $-4.831$  and  $-5.149$  for channel 15 of FY-3C/MWHS-2 and FY-3D/MWHS-2, respectively). The PDFs of the first-guess departure of channels 2–4, which were not sensitive to clouds or rain, could basically meet the Gaussian distribution requirements of 3DVAR (Figure 3a,e). After applying the observation error model, the PDFs of the first-guess departures of all used channels conformed better to the Gaussian distribution. The skewness values of the PDF became much smaller (e.g., for channel 15, the skewness values of the PDFs were  $-0.629$  and  $-0.309$  for the FY-3C/MWHS-2 and FY-3D/MWHS-2 observations, respectively), and the kurtosis was also dramatically decreased. Apparently, the PDFs of the first-guess departures of the FY-3D/MWHS-2 observations after normalization approached the Gaussian distribution, with skewness and kurtosis values closer to zero than those of FY-3C/MWHS-2, and this could lead to the better performances of the quality control processes [52].

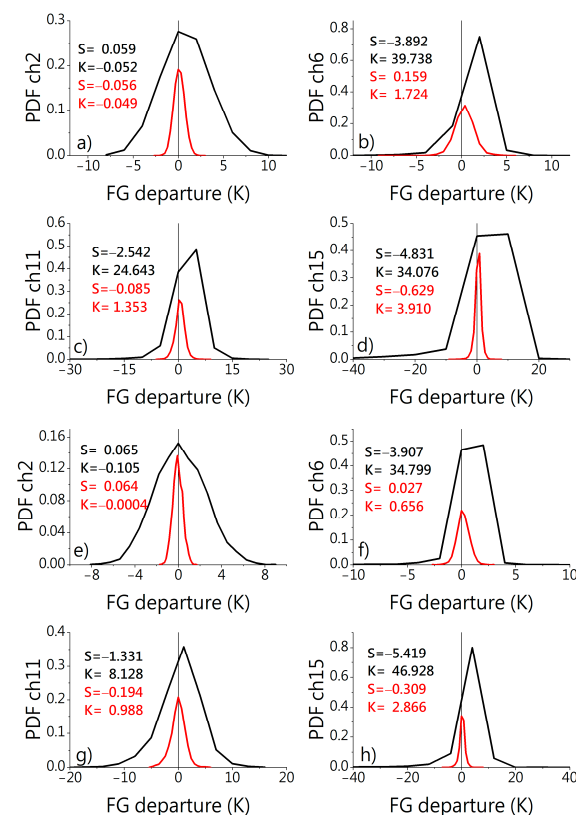


**Figure 3.** The probability distribution functions (PDFs) of the first-guess departures of the MWHS-2 data under all-sky conditions in terms of the absolute brightness temperatures without normalization (black lines) and with normalization (red lines) by the observation error model for FY-3C (a–d) and FY-3D (e–h) on 2 August 2020 before the quality control processes. S is skewness and K is kurtosis.

## 4. Results and Discussion

### 4.1. Assimilating Impacts

Figure 4 shows the spatial distribution of the first-guess departures (OMB) and the analysis departures (OMA) of FY-3D/MWHS-2 at 0000 UTC on 2 August for channel 11 as an example in the 3D-CLEAR and 3D-ALLSKY experiments after the thinning, bias correction and quality control processes, and the colored dots in the figures represent the OMB and OMA values.

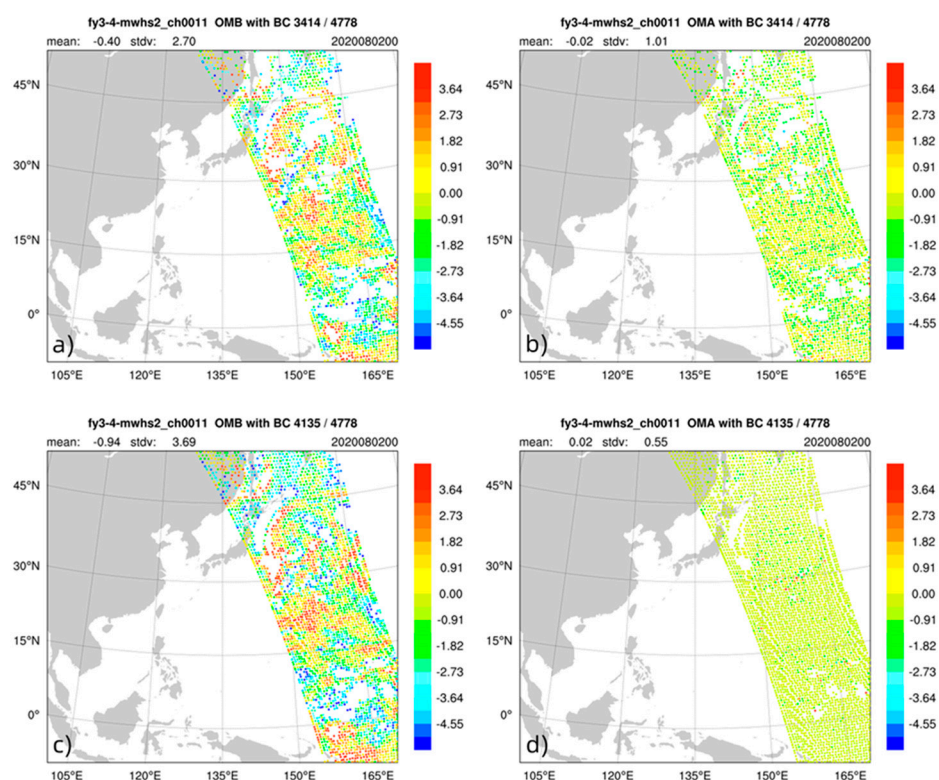


**Figure 4.** Spatial distributions of the OMBs (a,c) and OMAs (b,d) of the assimilated FY-3D/MWHS-2 observations of channel 11 at 0000 UTC on 2 August 2020 in 3D-CLEAR (a,b) or 3D-ALLSKY (c,d). The colored dots represent the OMB and OMA values (units: K).

The number of observation FY-3D/MWHS-2 pixels corresponding to channel 11 before quality control was approximately 4778 at 0000 UTC on 2 August for one footprint in a 6 h cycle, while the number of assimilated observations after quality control was 4135 under all-sky conditions; however, only 3414 pixels were used under clear-sky conditions, evidently confirming that the all-sky approach could make sufficient use of the observations.

The OMBs were significantly reduced after the bias correction and quality control processes, and most absolute OMA values were approximately zero under both clear-sky and all-sky conditions. Although the standard deviations of the OMBs were generally larger under all-sky conditions than under clear-sky conditions, the standard deviations of the OMAs were smaller for the former, suggesting that the analysis fields were much closer to the observations than the background, even when more data were assimilated.

To further understand the data usage when the two microwave humidity sounding observation groups are combined, the spatial coverage of the MWHS-2 data from the two Fengyun-3 satellites in CD experiments are displayed in Figure 5; the background image is the 1 h average brightness temperature products from Stretched Visible and Infrared Spin Scan Radiometer-2 of FengYun-2G (FY-2G/VISSR-2) over one 6 h cycle. In the CD-CLEAR results (Figure 5a), the green dots represent the FY-3C/MWHS-2 observation pixels and the blue dots represent the FY-3D/MWHS-2 observation pixels under clear-sky conditions. The yellow (FY-3C/MWHS-2) and red (FY-3D/MWHS-2) dots represent the additional

observation pixels added in the CD-ALLSKY experiment (Figure 5b). Convincingly, the data utilization of CD-ALLSKY was quite high, and the increased observation pixels were located mostly in the thick-cloud-covered areas, including the key typhoon regions. The combined data usage from the two Fengyun-3 satellites applied a tighter constraint for the truth values, and this could lead to a better fitting effect; in addition, these extra observations under all-sky conditions potentially positively impacted the typhoon predictions.

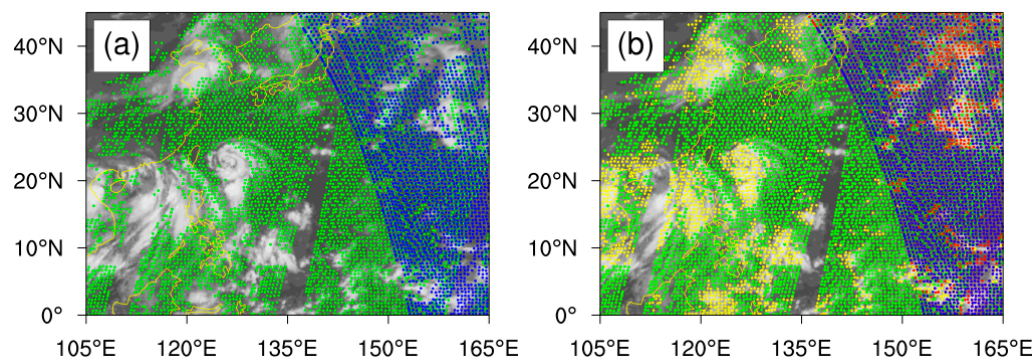


**Figure 5.** The coverage of the FY-3C/MWHS-2 observations (the green points represent the data collected under clear-sky conditions, and the yellow points represent the additional data collected over cloudy areas) and FY-3D/MWHS-2 observations (the blue points represent the data collected under clear-sky conditions, and the red points represent the additional data obtained in cloudy regions) in the CD-CLEAR (a) and CD-ALLSKY (b) experiments with the FY-2G satellite brightness temperature product derived from the Stretched Visible and Infrared Spin Scan Radiometer-2 of FY-2G (FY-2G/VISSR-2) at 0000 UTC on 2 August 2020.

#### 4.2. Prediction Impacts

##### 4.2.1. Independent Impacts of Assimilating FY-3C/MWHS-2 and FY-3D/MWHS-2 Observations

The best-track data from the JMA were used to verify the simulated typhoon tracks of Hagupit from the CON, 3C-CLEAR, 3C-ALLSKY, 3D-CLEAR and 3D-ALLSKY experiments, and the track errors of the forecasts referring to the JMA best-track data were calculated quantitatively (Figure 6). Compared to the track predicted in the CON experiment, all assimilating experiments showed apparently positive impacts (better approaching the best track) on the typhoon-track predictions regardless of whether the Fengyun-3 satellite data or the data containing clouds after 12 h were assimilated or not. Basically, the all-sky experiments provided better-simulated typhoon tracks than the clear-sky runs, and 3C-ALLSKY displayed the best forecasts with the smallest track errors. The track errors of 3D-ALLSKY were slightly larger than those of 3C-ALLSKY but much smaller than those of the two experiments in which the MWHS-2 clear-sky data were assimilated. After the landfall of Hagupit, the track errors dropped sharply in both all-sky experiments starting from 1800 UTC on 3 August 2020 and gradually increased from 1200 UTC on 4 August 2020.

Hagupit was not very strong at its peak. However, due to the warm sea surface temperatures (SSTs) and sufficient water vapor transportation along its track region, Hagupit was characterized by rapid offshore intensification. Evidently, all experiments, including the control run and the assimilation experiments, overestimated the minimum sea level pressure (MSLP) referring to the JMA intensity data over the whole forecasting time period, especially when Typhoon Hagupit traveled over sea from 1200 UTC on 1 August 2020 to 0600 UTC on 5 August 2020 (Figure 7). In the experiments with FY-3C/MWHS-2 radiances, 3C-ALLSKY predicted a much closer MSLP to the JMA, but it was still 6 h earlier, and after 1800 UTC on 3 August 2020, the intensity and variations were improved and became quite similar to those of the JMA. The 3C-CLEAR results provided a basic intensity variation trend similar to that of JMA. In the FY-3D/MWHS-s assimilating experiments, the forecasting impacts of the typhoon intensity were essentially neutral in both the clear-sky and all-sky runs before landfall, but 3D-ALLSKY indicated a slight improvement after 1800 UTC on 3 August 2020.

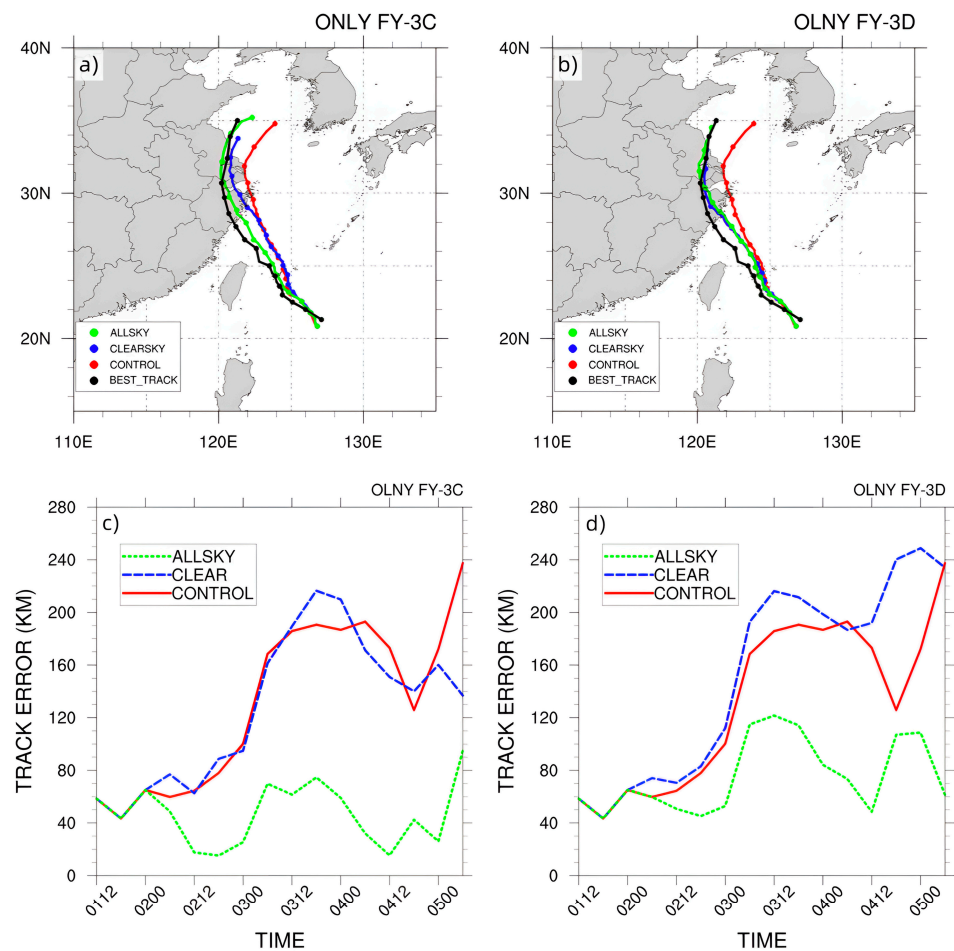


**Figure 6.** The predicted tracks (a,b) and the absolute track errors (c,d) of Hagupit from 1200 UTC 1 August 2020 to 0600 UTC 5 August 2020 from experiments with only assimilated FY-3C observations (a,c) and experiments with only assimilated FY-3D data (b,d). (interval: 6 h; black line: Japan Meteorological Agency best track; red line: CON; blue line: 3C-CLEAR and 3D-CLEAR; green line: 3C-ALLSKY and 3D-ALLSKY).

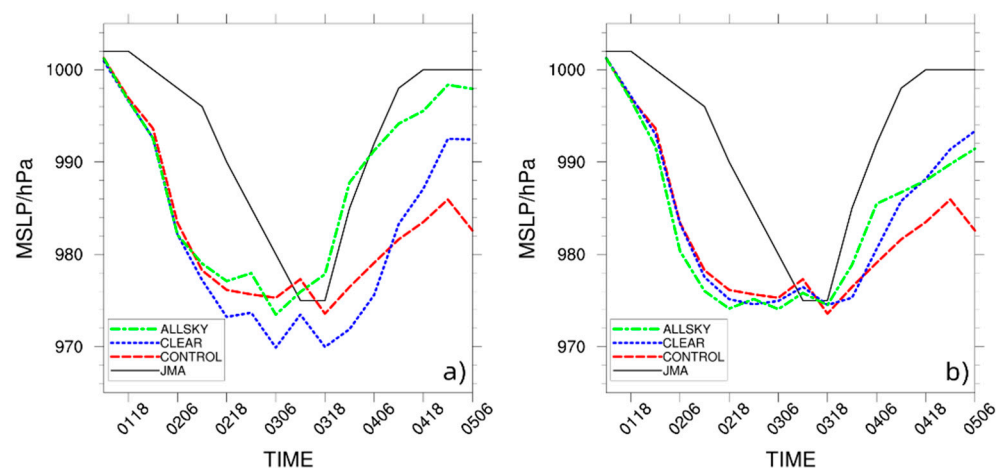


**Figure 7.** Time series of the MSLPs of Hagupit from 1200 UTC on 1 August 2020 to 0600 UTC on 5 August 2020, obtained while assimilating only FY-3C MWS-2 observations (a) and only FY-3D MWS-2 data (b) (unit: hPa; black line: JMA; red line: experiment CON; blue line: experiments 3C-CLEAR and 3D-CLEAR, respectively; green line: 3C-ALLSKY and 3D-ALLSKY). MSLP represents the minimum sea level pressure, and JMA is the Japan Meteorological Agency.

Since Hagupit made landfall on the night of 3 August, the 24 h accumulated precipitation distribution figures from 0000 UTC on 3 August to 0000 UTC on 5 August 2020 are displayed in Figure 8. The 24 h accumulated precipitation data obtained from the national meteorological stations of the China Meteorological Administration (CMA) were interpolated and used as a reference. Compared to the observations, heavy rainfall was falsely simulated occurring in southern China along the coastline in all simulations (not shown), and the assimilating experiments did not correct this error regardless of whether the instruments or data contained clouds in the whole forecasting period. For the 24 h accumulated precipitation forecast on 3 August, assimilating only 3C-ALLSKY observations caused a heavy rainstorm to be predicted over the east coast of China caused by the landfall of Hagupit, but this precipitation area was much narrower than the observations. The assimilating impacts were more evident over the next 24 h (4 August 2020), with improved precipitation amounts and locations appearing in the assimilating runs compared to the observations. Undoubtedly, the all-sky experiments provided better precipitation forecasts than the clear-sky experiments, and the heavy precipitation over the east coast of China improved much more alongside the two heavy rainfall centers predicted in 3D-ALLSKY (Figure 8d) compared to only the single center predicted in 3C-ALLSKY (Figure 8b); this difference may have been due to the assimilation of additional FY-3D/MWHS-2 radiance data allowing a better fitting to be obtained with time.

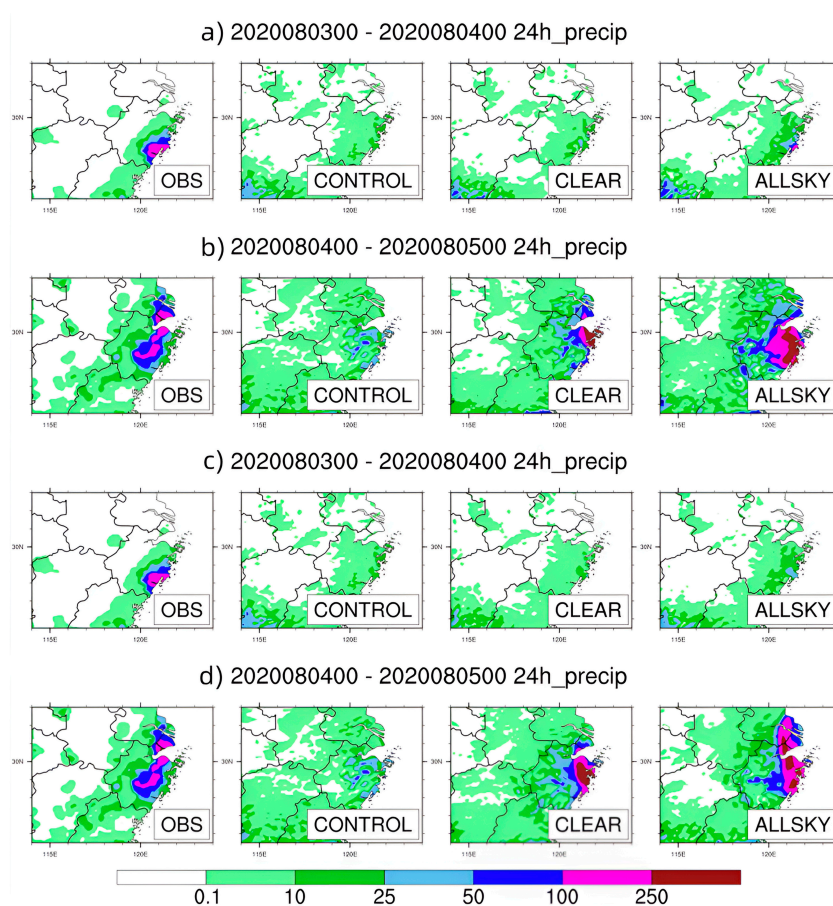


**Figure 8.** The 24 h accumulated precipitation (unit: mm) over land from 0000 UTC on 3 August and 0000 UTC on 5 August 2020 obtained in the experiments assimilating FY-3C/MWHS-2 observations only (a,b) and FY-3D/MWHS-2 data only (c,d). The precipitation observations were obtained from the national meteorological stations of the Chinese Meteorological Administration (CMA).

Dichotomous (yes–no) forecasts were used here to quantitatively evaluate the effectiveness of the precipitation forecasts. An event in the quantitative precipitation forecasts was defined as the conditions reaching a specified threshold at a given point. The probability of

detection (POD), false alarm ratio (FAR), bias, threat score (TS) and success ratio (SR) of each precipitation forecasting result set are shown in Figure 9 and were defined as follows:

$$POD = \frac{A}{A + C} \quad (6)$$

$$FAR = \frac{B}{A + B} \quad (7)$$

$$bias = \frac{A + B}{A + C} \quad (8)$$

$$TS = \frac{A}{A + B + C} \quad (9)$$

$$SR = 1 - FAR \quad (10)$$

where  $A$  represents the correct prediction of events,  $B$  represents events that were predicted but did not occur,  $C$  represents the events that were observed but not predicted and  $D$  represents the correct predictions of no event. The  $POD$ ,  $SR$ ,  $TS$  and  $bias$  results are shown simultaneously in the performance diagram [61]. Good predictions appear in the upper-right region of the diagram. In this study, the simulated precipitation predictions were interpolated into the observation stations in Zhejiang and Jiangsu provinces and in the Shanghai region, which were seriously affected by the landfall of Typhoon Hagupit. The  $TS$  scores were relatively high at low thresholds and mostly larger than 0.5 at 0.1 mm. For most members, the  $TS$  scores decreased as higher thresholds were approached. For the biases, distinct underpredictions were exhibited at bias values smaller than 0.5 in 3C-ALLSKY at 25 mm and above on 3 August (Figure 9a, green circle). Similar to the accumulated precipitation results, no members were present at 50 mm or above on 3 August in the 3D-ALLSKY experiment (Figure 9b, green circle) or in the other experiments. On 4 August, the members were more clustered in the 3D-ALLSKY experiment (Figure 9b, green triangle) than in the 3C-ALLSKY experiment (Figure 9a, green triangle). Although some overpredictions occurred in the 3D-ALLSKY experiment, the  $TS$  scores were still higher than those in the 3C-ALLSKY experiment.

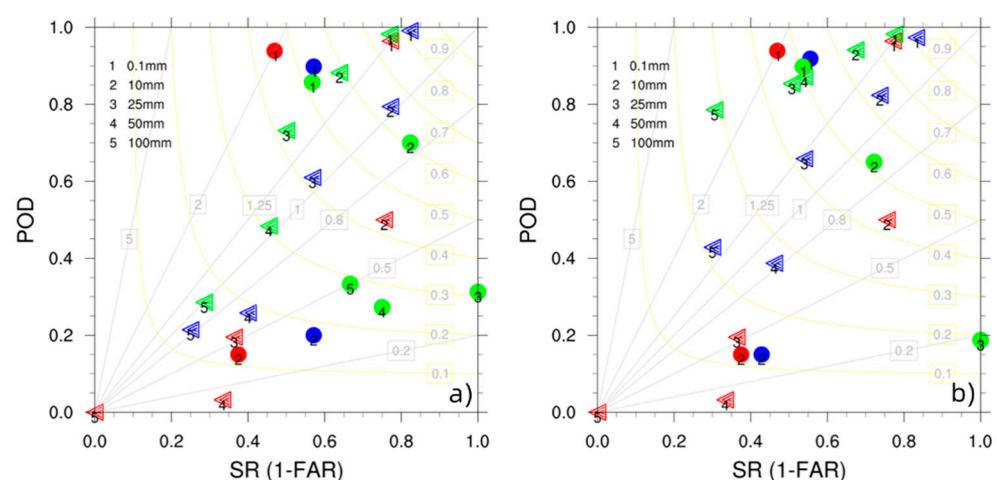


**Figure 9.** Performance diagram of 24 h accumulated precipitation from 0000 UTC on 3 August 2020 to 0000 UTC on 4 August 2020 (circle) and from 0000 UTC on 4 August 2020 to 0000 UTC on 5 August 2020 (triangle) obtained by assimilating only FY-3C MWHs-2 observations (a, red: CONTROL, blue: 3C-CLEAR, green: 3C-ALLSKY) and only FY-3D MWHs-2 data (b, red: CONTROL, blue: 3D-CLEAR, green: 3D-ALLSKY) at five selected thresholds from 0.1 to 100 mm (1: 0.1 mm, 2: 10 mm, 3: 25 mm, 4: 50 mm, and 5: 100 mm) in Zhejiang and Jiangsu provinces and in the Shanghai region.

The daily root mean square errors (RMSEs) of relative humidity, temperature and vector winds from 2 August 2020 to 5 August 2020 referring to the European Centre for Medium-Range Weather Forecasts (ECMWF) analysis (ERA5) data were calculated in the domain of the Hagupit track (110°E–135°E, 15°N–40°N) to quantitatively evaluate the assimilation impacts. Since the results of the experiments in which FY-3C/MWHS-2 and FY-3D/MWHS-2 observations were assimilated were similar, the RMSEs from the experiment in which FY-3D/MWHS-2 data were assimilated are shown as an example (Figure 10). Notably, the vertical RMSEs decreased most in the vector winds of the 3D-ALLSKY experiment, and the evidently positive impacts extended from 400 hPa to the surface starting from the 48 h forecasts (Figure 10h), consistent with the fact that the forecasts of the vector wind field were the most sensitive to the assimilation of microwave humidity sounding data [62]. The positive impacts of 3D-CLEAR on the physical variable field prediction were concentrated around the middle to upper levels of the atmosphere (i.e., 250 hPa to 650 hPa for relative humidity, 200 hPa to 500 hPa for temperature and 200 hPa to 300 hPa for vector winds), and these improvements exhibited with increased temporal variations. Further, 3D-CLEAR even performed better than 3D-ALLSKY in reducing the RMSEs of the relative humidity results but performed much worse in improving the vector wind RMSEs, while the two experiments showed comparable impacts on temperature. Apparently, both clear-sky and all-sky assimilations with FY-3D/MWHS-2 radiance data resulted in neutral to positive impacts on the physical variable predictions, and different variables showed different sensitivities to these assimilations. This kind of positive impact was more dominant when assimilating FY-3D/MWHS-2 observations than when assimilating FY-3C/MWHS-2 data (not shown), especially for the vector winds from the 48 h forecasts, which may benefit water vapor transport and be one reason for the lower TS score obtained in the 3C-ALLSKY experiment than in the 3D-ALLSKY experiment from 0000 UTC on 4 August and 0000 UTC on 5 August 2020.

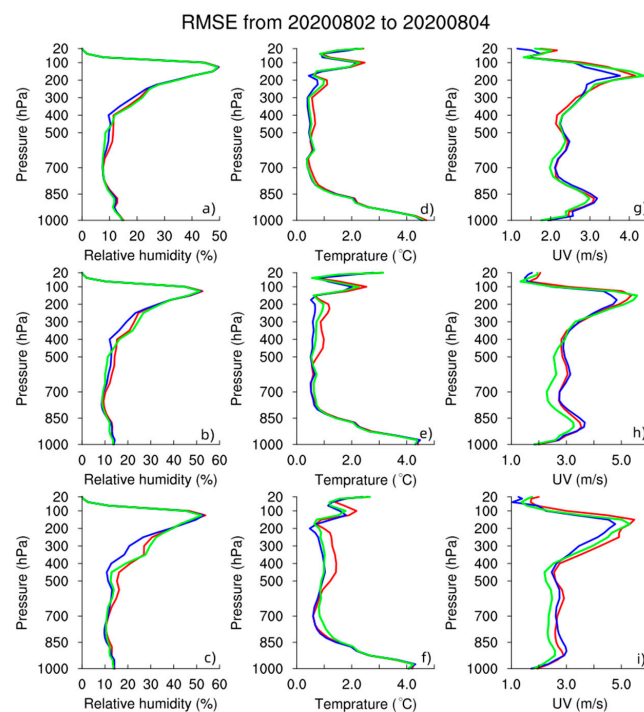


**Figure 10.** The vertical profiles of the daily (24 h) forecast root mean square errors (RMSEs) of relative humidity (a–c, unit: %), temperature (d–f, unit: K) and vector winds (g–i, unit: m/s) on 2 August (top), 3 August (middle) and 4 August (bottom) in 2020 referring to the European Centre for Medium-Range Weather Forecasts analysis (ERA5) data from the FY-3D/MWHS-2 data assimilation experiments. (Red line: CON; blue line: 3D-CLEAR; green line: 3D-ALLSKY).

#### 4.2.2. Combined Impacts of Assimilating the MWHS-2 Observations of Both FY-3C and FY-3D

The forecasting results described above effectively demonstrate that directly assimilating MWHS-2 radiance data from different Fengyun-3 satellites differently impacts the typhoon predictions. With different orbits and equatorial cross times (ECTs), the MWHS-2 observations from FY-3C and FY-3D can complement each other and improve the data usage in WRFDA. Therefore, the combined impacts of assimilating MWHS-2 observations from both FY-3C and FY-3D on the Typhoon Hagupit predictions are discussed in the following paragraphs.

Apparently, CD-ALLSKY provides the best typhoon-track forecasts for Hagupit (Figure 11), with much more accurate landfall locations; the smallest track errors obtained in this experiment were below 50 km, lower than those obtained in the CD-CLEAR and control runs, especially before 0600 UTC on 4 August 2020. After 0600 UTC on 4 August 2020, the tracks predicted by 3C-ALLSKY and 3D-ALLSKY outperformed those predicted by CD-ALLSKY over land (Figure 11a). The predicted track in the CD-CLEAR experiment visually approached the best track; however, with the relatively slow moving speeds of Hagupit in this experiment, the track errors were actually very large, even larger than the control errors. The reason for these increasing track errors over land after 0600 UTC on 4 August 2020 in the CD-ALLSKY experiment needs further investigation since forecasting typhoons over land is more difficult than forecasting typhoons over water due to various reasons. In addition, the variation tendency of the CD-ALLSKY-predicted typhoon intensity was similar to that of the JMA data, but the smallest MSLP appeared almost 18 h earlier, while the MSLP predicted in the CD-CLEAR experiment was lower than that predicted in the all-sky assimilation experiment.

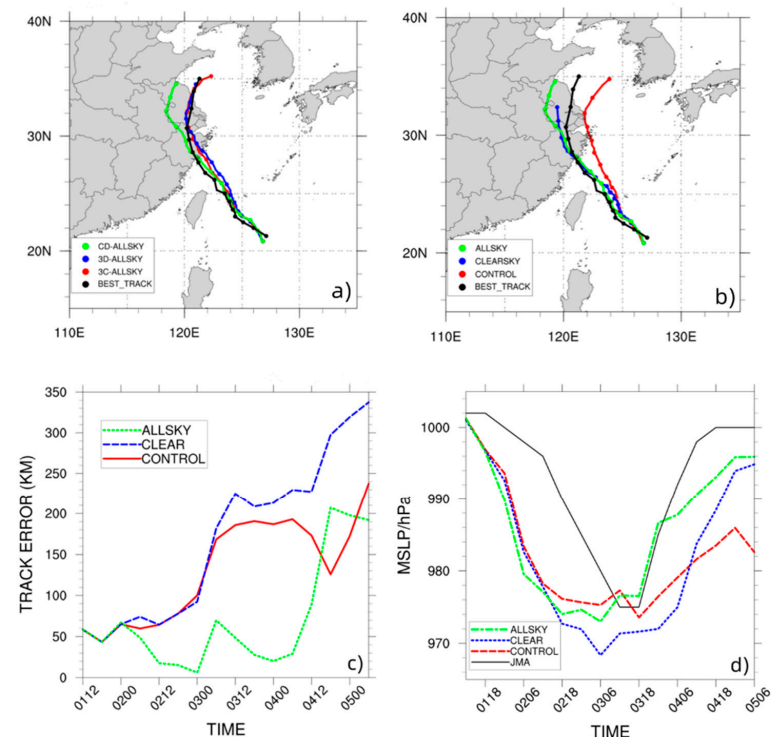


**Figure 11.** The Hagupit tracks predicted in the all-sky experiments (a) (black line: Japan Meteorological Agency best track; red line: 3C-ALLSKY; blue line: 3D-ALLSKY; green line: CD-ALLSKY) and the Hagupit tracks predicted in the CON (red line), CD-CLEAR (blue line) and CD-ALLSKY (green line) experiments along with the JMA best track (black line) (b); the absolute track errors obtained in the CON (red line), CD-CLEAR (blue line) and CD-ALLSKY (green line) experiments in reference to the JMA best track (c); and the Hagupit intensity variations with time (d) from 1200 UTC on 1 August 2020 to 0600 UTC on 5 August 2020 from the CON (red line), CD-CLEAR (blue line) and CD-ALLSKY (green line) experiments compared to the JMA best-track data (black line).

Although the false precipitation predictions over the coastline in southern China were not eliminated in the assimilation experiments, the locations and amounts of heavy rainfall triggered by the landfall of Hagupit were predicted best in the CD-ALLSKY experiment, while the CD-CLEAR experiment omitted the rainstorm in the first 24 h forecast after landfall (figures not shown). The results of the equitable threat score (ETS), which represents an improved TS score, are shown in Figure 12 to further evaluate the impacts of assimilating MWS-2 data in Zhejiang, Jiangsu and Shanghai provinces. The ETS is defined as follows:

$$ETS = \frac{A - \frac{(A+B) \times (A+C)}{A+B+C+D}}{A + B + C - \frac{(A+B) \times (A+C)}{A+B+C+D}} \quad (11)$$

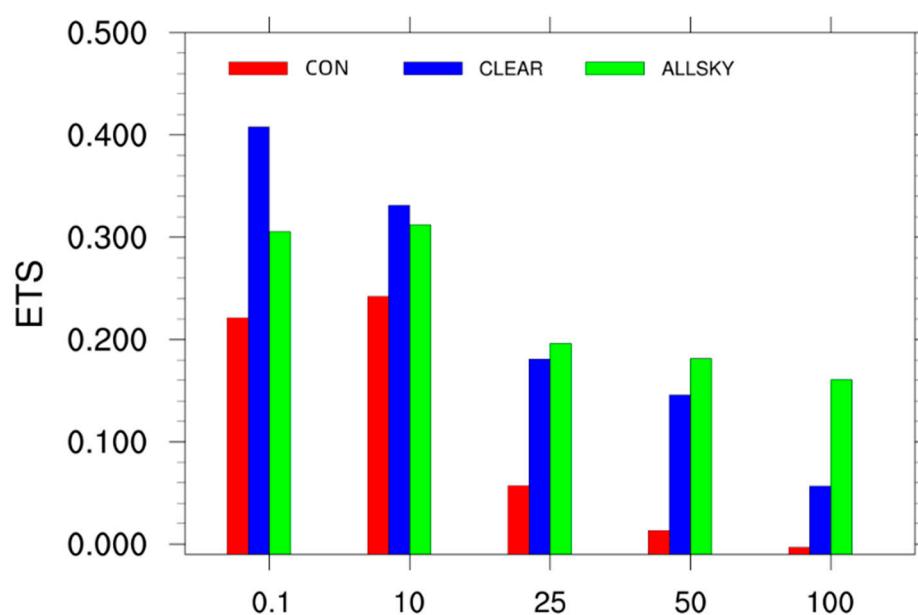


**Figure 12.** The equitable threat scores (ETSs) of the 24 h accumulated precipitation from 0000 UTC on 3 August to 0000 UTC on 5 August 2020 in the CON (red), CD-CLEAR (blue) and CD-ALLSKY (green) experiments at 0.1, 10, 25, 50 and 100 mm rainfall thresholds in Zhejiang and Jiangsu provinces and in the Shanghai region.

The ETSs were greatly improved in the CD-CLEAR and CD-ALLSKY experiments compared to the CON experiment at all thresholds. CD-ALLSKY made much more accurate predictions of heavy rainfall (>25 mm) than CD-CLEAR.

Evidently, assimilating both FY-3C/MWS-2 and FY-3D/MWS-2 observations can improve the forecasts the most because more high-quality data are used in the WRFDA system, allowing a better fit to be obtained for the subsequent analysis.

#### 4.2.3. Sensitivity to the Channel Selection

In the experiments described above, we did not distinguish between the assimilated observations from the 118 GHz and 183 GHz channels. As is known, 118 GHz (channels 2–7 are used in this study) and 183 GHz (channels 11–12 and 15 are used in this study) are sensitive to the oxygen- and water vapor-absorbing bands, respectively, and have different sensitivities to clouds and rain, resulting in the different impacts of considering these bands. Therefore, six additional all-sky experiments (i.e., 3C/D-118CH, 3C/D-183CH, CD-118CH and CD-183CH) were set up to discuss the assimilation sensitivities to the selected channels. All six runs had the exact same settings as the previous all-sky experiments, except that radiances only from either the 118 GHz channels or 183 GHz channels were assimilated.

Figure 13 presents the impacts of the channel selection on the track forecasts of Typhoon Hagupit in the all-sky assimilation experiments assimilating either the observations from the 118 GHz channels or the 183 GHz channels of the two FY-3 polar-orbit satellites.

Interestingly, compared to the JMA-derived best track after landfall, the tracks deviate towards inland China when only observations from the 118 GHz channels were assimilated regardless of which satellite provided the data, while the tracks deflected seaward when radiances only from the 183 GHz channels were assimilated. The 3D-118CH-simulated track deviated more inland than that of 3C-118CH, and the CD-118CH-simulated track deviated the most inland, but the CD-183CH-simulated track deflected seaward the least, illustrating that the more observations were assimilated, the more error growth was reflected in the temporal evolution results. Further studies are surely needed to investigate whether these performances indicate an impacting pattern due to channel selection or are just the incidental result of using ensemble or hybrid data assimilations, as this is beyond the scope of this report and is not discussed here.

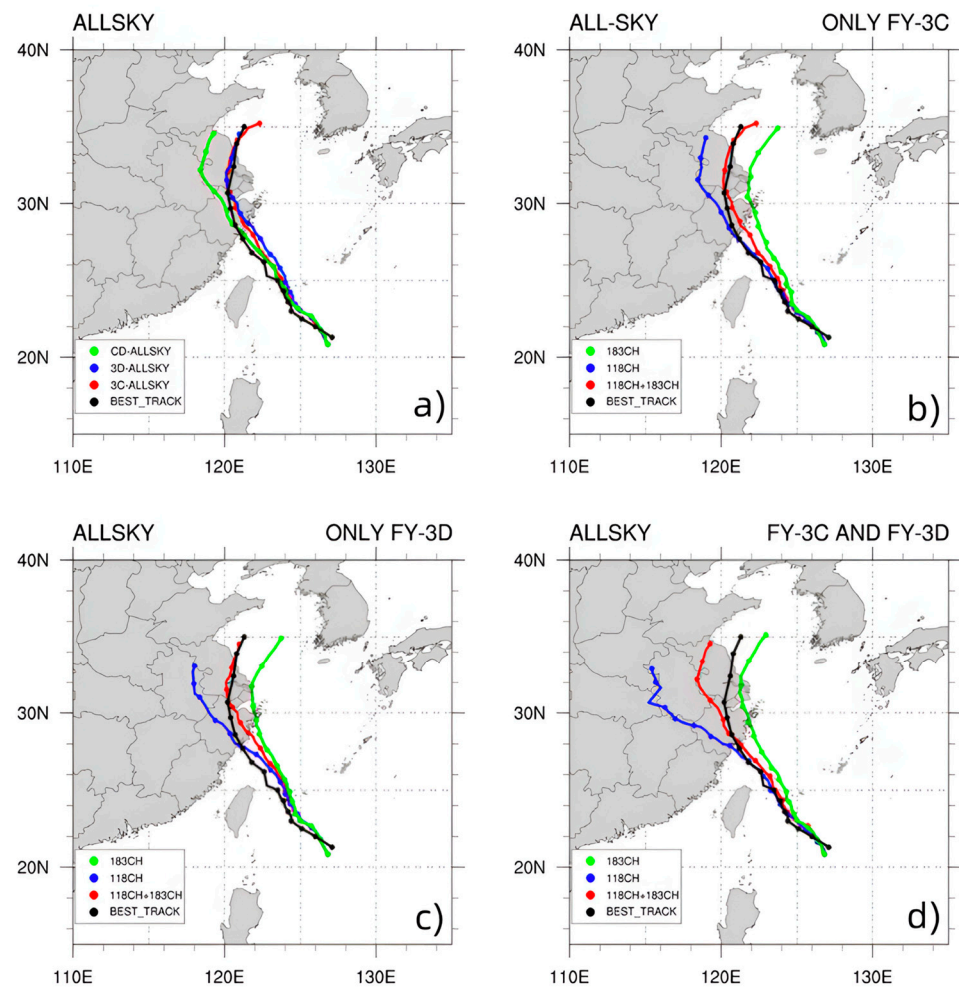


**Figure 13.** The predicted tracks of Hagupit from 1200 UTC on 1 August 2020 to 0600 UTC on 5 August 2020 from all-sky experiments (a) assimilating data from both the 118 GHz and 183 GHz channels (interval: 6 h; black line: Japan Meteorological Agency best track; red line: 3C-ALLSKY; blue line: 3D-ALLSKY; green line: CD-ALLSKY), (b) assimilating data only from FY-3C/MWHS-2 (black line: JMA best track; red line: 3C-ALLSKY; blue line: 3C- 118CH; green line: 3C- 183CH), (c) assimilating data only from FY-3D/MWHS-2 (black line: JMA best track; red line: 3D-ALLSKY; blue line: 3D- 118CH; green line: 3D- 183CH) and (d) assimilating data from both FY-3C/MWHS-2 and FY-3D/MWHS-2 (black line: JMA best track; red line: CD-ALLSKY; blue line: CD- 118CH; green line: CD- 183CH).

The time series of the absolute track errors of Hagupit compared to the JMA-reported best-track data from the all-sky channel-selection assimilation experiments are displayed in Figure 14. As expected, the track errors were smallest when the radiances from both the 118

GHz and 183 GHz channels were directly assimilated together in each all-sky experiment group; however, the track errors began to rise at 0600 UTC on 4 August 2020 in the CD-ALLSKY experiment and became larger than the CD-183CH errors 18 h later but were still much smaller than those obtained in the CD-118CH experiment. Although the track errors obtained in 3D-ALLSKY were smaller than those obtained in 3C-ALLSKY, among the errors obtained in all three experiments, the errors obtained by assimilating the 183 GHz channels only were quite comparable with each other. Different results were found in the experiments that assimilated data from only the 118 GHz channel; the track errors increased remarkably around the time of landfall (before or after 1930 UTC on 3 August 2020) after remaining lower than those of the all-sky assimilation experiments using only the 183 GHz channel data in each experimental group. Notably, the errors rose most significantly in the CD-118CH experiment, and the possible cause for this is discussed above.

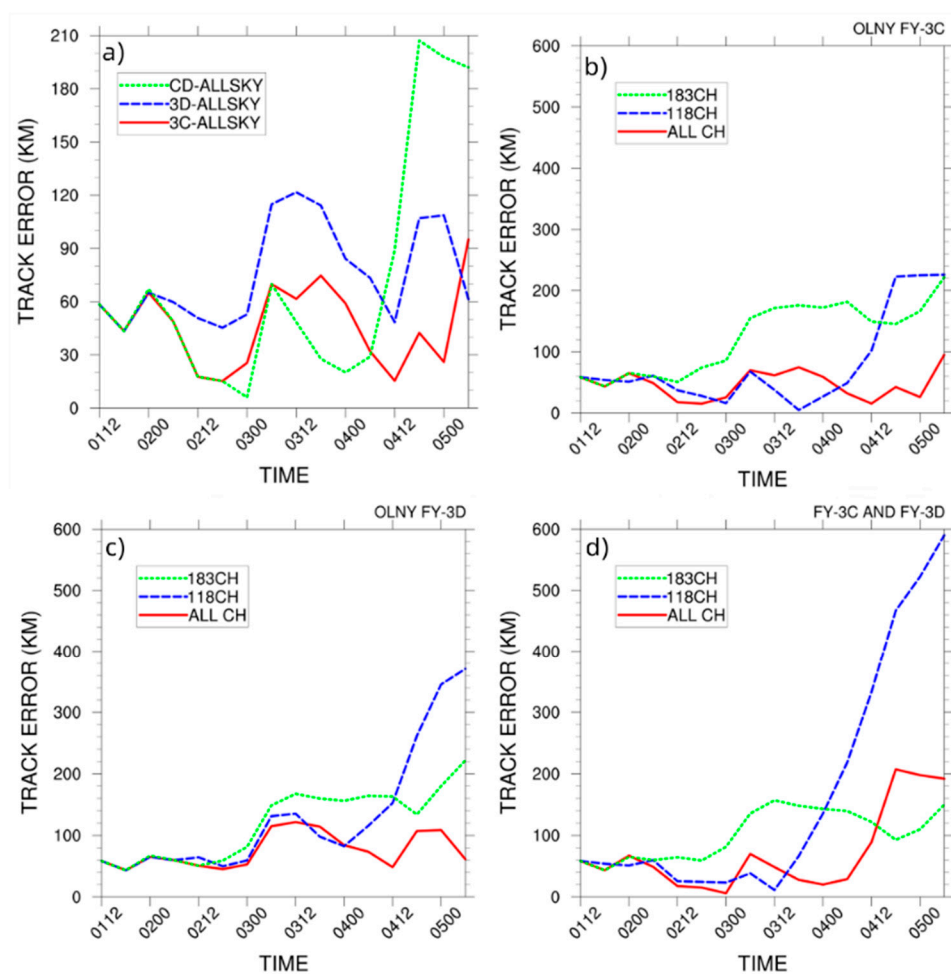


**Figure 14.** The time series of the absolute track errors of Hagupit from 1200 UTC on 1 August 2020 to 0600 UTC on 5 August 2020 compared to the JMA-derived best-track data from all-sky experiments (a) assimilating data from both the 118 GHz and 183 GHz channels (unit: km; red line: 3C-ALLSKY; blue line: 3D-ALLSKY; green line: CD-ALLSKY), (b) assimilating data only from FY-3C/MWHS-2 (red line: 3C-ALLSKY; blue line: 3C-ALLSKY-118CH; green line: 3C-ALLSKY-183CH), (c) assimilating data only from FY-3D/MWHS-2 (red line: 3D-ALLSKY; blue line: 3D-ALLSKY-118CH; green line: 3D-ALLSKY-183CH) and (d) assimilating data from both FY-3C/MWHS-2 and FY-3D/MWHS-2 (red line: CD-ALLSKY; blue line: CD-ALLSKY-118CH; green line: CD-ALLSKY-183CH).

## 5. Conclusions

This study was the first to assimilate FY-3D/MWHS-2 observations under clear, cloudy and rainy conditions while employing the updated WRFDA system with an all-sky assimilation capacity. A series of experiments in which MWHS-2 data from different satellites

(i.e., FY-3C and FY-3D) or both satellites were assimilated were carried out to evaluate the impacts of the FY-3D/MWHS-2 observations on the typhoon predictions.

A symmetric observation error model that inputs the cloud coverage as a predictor to assign observation errors to cloud- and precipitation-affected observations could effectively transform the highly non-Gaussian PDFs of the OMBs to meet the data assimilation requirements. When additional cloud- and precipitation-affected observations were assimilated, significantly improved performances were achieved in terms of the forecasted relative humidity, temperature and wind fields around Typhoon Hagupit, resulting in better predictions of the track and intensity of Hagupit. On the other hand, the forecast performances obtained after assimilating MWHS-2 observations from different satellites were comparable; the impacts of jointly assimilating MWHS-2 observations from both the FY-3C and FY-3D satellites on the typhoon forecasts were generally neutral to evidently positive, and this experiment resulted in the best landfall location forecast. Therefore, since the state-of-the-art model was not included in the assimilation experiments performed in this study, for underdeveloped regions, even without dense conventional data, Fengyun-3-series satellite observations can be reliable and important data sources for regional NWP, and NWP can greatly benefit from the collaborative assimilation of data from multiple meteorological satellites.

The effects of the sensitivities of the 118 GHz and 183 GHz channels from the MWHS-2 data on the typhoon predictions were also assessed. The assimilation of only the 118 GHz or 183 GHz channels resulted in a generally worse forecast performance than the results obtained when utilizing both channels. The forecast degradation resulting from assimilating only the 118 GHz channels occurred when Typhoon Hagupit made landfall and moved inland, while the 183 GHz-channel assimilation experiment caused the Hagupit track to move toward the ocean over its lifetime. In other words, the impacts resulting from assimilating the 118 GHz or 183 GHz channels only on the Hagupit track showed evidently opposite results. In the future, the ensemble assimilation technique can be used to investigate whether these performances were the result of the channel selection or just incidental. In the future, FY-4 will be made to carry microwave instruments, which may be the first of such instruments in the world to be carried on a geosynchronously orbiting satellite. This will improve the temporal resolution of microwave observations and may improve the accuracy of NWPs. In addition, a more advanced vortex initialization of the HWRF model will be studied, which may facilitate better intensification and movement predictions of typhoons [19]. Therefore, performing numerical experiments with different NWP models, different satellite data and different assimilation techniques is necessary in further research.

**Author Contributions:** To complete this study, all authors make a good effort and should be thanked. The contributions of K.C. are conceptualization, supervision, writing—review and editing, project administration and funding acquisition; Z.C. contributed to the software, data curation, writing—original draft preparation, formal analysis and visualization. Z.X. is responsible for the software, investigation and writing—review and editing. G.L. contributed to the validation. All authors have read and agreed to the published version of the manuscript.

**Funding:** The authors appreciate the National Natural Science Foundation of China to support this research through Grant No. 41875039 and also thank the National Key Scientific and Technological Infrastructure project “Earth System Science Numerical Simulator Facility” (EarthLab) for its support (Grant No.:2022-EL-PT-00052).

**Data Availability Statement:** The FY-3 series MWHS-2 data and FY-2G brightness temperature product are obtained freely from the official website of National Satellite Meteorological Center (NSMC) (<http://satellite.nsmc.org.cn/portalsite/Data/DataView.aspx/>, accessed on 19 September 2022). The ECMWF analysis and the NCEP reanalysis data can be downloaded from their official websites (<https://cds.climate.copernicus.eu/cdsapp#!/dataset/reanalysis-era5-pressure-levels>, accessed on 19 September 2022) and (<https://rda.ucar.edu/datasets/ds083.3/>, accessed on 21 September 2021), respectively. The precipitation observations can be obtained from CMA website (<http://data.cma.cn/data/cdcindex/cid/f0fb4b55508804ca.html/>, accessed on 19 September 2022).

**Acknowledgments:** The authors acknowledge the funding supporters and the data providers for the research supports and help. The authors also thank Alan Geer for his always kind advice and encouragement.

**Conflicts of Interest:** The authors declare no conflict of interest.

## References

1. Bauer, P.; Moreau, E.; Chevallier, F.; O'keeffe, U. Multiple-scattering microwave radiative transfer for data assimilation applications. *Q. J. R. Meteorol. Soc.* **2006**, *132*, 1259–1281. [CrossRef]
2. Bauer, P.; Geer, A.J.; Lopez, P.; Salmond, D. Direct 4D-Var assimilation of all-sky radiances. Part I: Implementation. *Q. J. R. Meteorol. Soc.* **2010**, *136*, 1868–1885. [CrossRef]
3. Wylie, D.P.; Menzel, W.P. Eight years of high cloud statistics using HIRS. *J. Clim.* **1999**, *12*, 170–184. [CrossRef]
4. Kim, M.-J.; English, S.; Bauer, P.; Geer, A.; Okamoto, K. Comparison of Progress in Assimilating Cloud-Affected Microwave Radiances at NCEP, ECMWF, JMA and the Met Office. Visiting Scientist Mission Report, NWP SAF EUMETSAT, 23th, Oct 2008. 2008. Available online: [https://www.nwpsaf.eu/publications/vs\\_reports/nwpsaf-mo-vs-037.pdf](https://www.nwpsaf.eu/publications/vs_reports/nwpsaf-mo-vs-037.pdf) (accessed on 16 March 2023).
5. McNally, A. A note on the occurrence of cloud in meteorologically sensitive areas and the implications for advanced infrared sounders. *Q. J. R. Meteorol. Soc. A J. Atmos. Sci. Appl. Meteorol. Phys. Oceanogr.* **2002**, *128*, 2551–2556. [CrossRef]
6. Geer, A.J.; Bauer, P. Observation errors in all-sky data assimilation. *Q. J. R. Meteorol. Soc.* **2011**, *137*, 2024–2037. [CrossRef]
7. Lawrence, H.; Bormann, N.; Lu, Q.; Geer, A.; English, S. *An Evaluation of FY-3C MWHS-2 at ECMWF*; EUMETSAT/ECMWF Fellowship Programme Research Report; ECMWF: Reading, UK, 2015; Volume 37, Available online: <https://status.ecmwf.int/en/elibrary/75346-evaluation-fy-3c-mwhs-2-ecmwf> (accessed on 16 March 2023).
8. Hong, S.-Y.; Noh, Y.; Dudhia, J. A new vertical diffusion package with an explicit treatment of entrainment processes. *Mon. Weather Rev.* **2006**, *134*, 2318–2341. [CrossRef]
9. Geer, A.J.; Bauer, P.; English, S.J. *Assimilating AMSU-A Temperature Sounding Channels in the Presence of Cloud and Precipitation*; ECMWF Technical Memoranda 670; European Centre for Medium-Range Weather Forecasts: Reading, UK, 2012.
10. Wattrelot, E.; Caumont, O.; Mahfouf, J.-F. Operational implementation of the 1D+ 3D-Var assimilation method of radar reflectivity data in the AROME model. *Mon. Weather Rev.* **2014**, *142*, 1852–1873. [CrossRef]
11. Kazumori, M.; Geer, A.J.; English, S.J. Effects of all-sky assimilation of GCOM-W/AMSR2 radiances in the ECMWF numerical weather prediction system. *Q. J. R. Meteorol. Soc.* **2016**, *142*, 721–737. [CrossRef]
12. Forbes, R.; Geer, A.; Lonitz, K.; Ahlgrimm, M. Reducing systematic errors in cold-air outbreaks. *ECMWF Newsl.* **2016**, *146*, 17–22.
13. Geer, A.; Ahlgrimm, M.; Bechtold, P.; Bonavita, M.; Bormann, N.; English, S.; Fielding, M.; Forbes, R.; Hogan, R.; Hólm, E. *Assimilating Observations Sensitive to Cloud and Precipitation*; ECMWF Technical Memoranda 815; European Centre for Medium-Range Weather Forecasts: Reading, UK, 2017.
14. Martinet, P.; Fourrié, N.; Guidard, V.; Rabier, F.; Montmerle, T.; Brunel, P. Towards the use of microphysical variables for the assimilation of cloud-affected infrared radiances. *Q. J. R. Meteorol. Soc.* **2013**, *139*, 1402–1416. [CrossRef]
15. Okamoto, K. Assimilation of overcast cloudy infrared radiances of the geostationary MTSAT-1R imager. *Q. J. R. Meteorol. Soc.* **2013**, *139*, 715–730. [CrossRef]
16. Migliorini, S.; Lorenc, A.C.; Bell, W. A moisture-incrementing operator for the assimilation of humidity-and cloud-sensitive observations: Formulation and preliminary results. *Q. J. R. Meteorol. Soc.* **2018**, *144*, 443–457. [CrossRef]
17. Geer, A.J.; Lonitz, K.; Weston, P.; Kazumori, M.; Okamoto, K.; Zhu, Y.; Liu, E.H.; Collard, A.; Bell, W.; Migliorini, S.; et al. All-sky satellite data assimilation at operational weather forecasting centres. *Q. J. R. Meteorol. Soc.* **2018**, *144*, 1191–1217. [CrossRef]
18. Duncan, D.I.; Bormann, N.; Geer, A.J.; Weston, P. Assimilation of AMSU-A in All-Sky Conditions. *Mon. Weather Rev.* **2022**, *150*, 1023–1041. [CrossRef]
19. Dodla, V.B.; Desamsetti, S.; Yerramilli, A. A comparison of HWRF, ARW and NMM models in Hurricane Katrina (2005) simulation. *Int. J. Environ. Res. Public Health* **2011**, *8*, 2447–2469. [CrossRef]
20. Sawada, M.; Ma, Z.; Mehra, A.; Tallapragada, V.; Oyama, R.; Shimoji, K. Impacts of assimilating high-resolution atmospheric motion vectors derived from Himawari-8 on tropical cyclone forecast in HWRF. *Mon. Weather Rev.* **2019**, *147*, 3721–3740. [CrossRef]
21. Lewis, W.E.; Velden, C.S.; Stettner, D. Strategies for assimilating high-density atmospheric motion vectors into a regional tropical cyclone forecast model (HWRF). *Atmosphere* **2020**, *11*, 673. [CrossRef]
22. Sawada, M.; Ma, Z.; Mehra, A.; Tallapragada, V.; Oyama, R.; Shimoji, K. Assimilation of Himawari-8 rapid-scan atmospheric motion vectors on tropical cyclone in HWRF system. *Atmosphere* **2020**, *11*, 601. [CrossRef]
23. Lim, A.H.; Nebuda, S.E.; Jung, J.A.; Daniels, J.M.; Bailey, A.; Bresky, W.; Bi, L.; Mehra, A. Optimizing the Assimilation of the GOES-16/-17 Atmospheric Motion Vectors in the Hurricane Weather Forecasting (HWRF) Model. *Remote Sens.* **2022**, *14*, 3068. [CrossRef]
24. Lu, X.; Davis, B.; Wang, X. Improving the Assimilation of Enhanced Atmospheric Motion Vectors for Hurricane Intensity Predictions with HWRF. *Remote Sens.* **2022**, *14*, 2040. [CrossRef]

25. Feng, J.; Qin, X.; Wu, C.; Zhang, P.; Yang, L.; Shen, X.; Han, W.; Liu, Y. Improving typhoon predictions by assimilating the retrieval of atmospheric temperature profiles from the FengYun-4A's Geostationary Interferometric Infrared Sounder (GIIRS). *Atmos. Res.* **2022**, *280*, 106391. [[CrossRef](#)]
26. Wu, T.-C.; Zupanski, M.; Grasso, L.D.; Kummerow, C.D.; Boukabara, S.-A. All-sky radiance assimilation of ATMS in HWRF: A demonstration study. *Mon. Weather Rev.* **2019**, *147*, 85–106. [[CrossRef](#)]
27. Skamarock, W.C.; Klemp, J.B.; Dudhia, J. A Description of the Advanced Research WRF Version 3. Available online: [https://www2.mmm.ucar.edu/wrf/users/docs/attic/arw\\_v3\\_bw.pdf](https://www2.mmm.ucar.edu/wrf/users/docs/attic/arw_v3_bw.pdf) (accessed on 16 March 2023).
28. Singh, R.; Kishtawal, C.; Pal, P.; Joshi, P. Improved tropical cyclone forecasts over north Indian Ocean with direct assimilation of AMSU-A radiances. *Meteor. Atmos. Phys.* **2012**, *115*, 15–34. [[CrossRef](#)]
29. Liu, Z.; Schwartz, C.S.; Snyder, C.; Ha, S.-Y. Impact of assimilating AMSU-A radiances on forecasts of 2008 Atlantic tropical cyclones initialized with a limited-area ensemble Kalman filter. *Mon. Weather Rev.* **2012**, *140*, 4017–4034. [[CrossRef](#)]
30. Xu, D.; Shu, A.; Shen, F.; Min, J.; Li, H.; Xia, X. Impacts of Multiple Radiance Data Assimilation on the Simulation of Typhoon Chan-Hom. *Atmosphere* **2020**, *11*, 957. [[CrossRef](#)]
31. Xu, D.; Huang, X.-Y.; Wang, H.; Mizzi, A.P.; Min, J. Impact of assimilating radiances with the WRFDA ETKF/3DVAR hybrid system on prediction of two typhoons in 2012. *J. Meteorol. Res.* **2015**, *29*, 28–40. [[CrossRef](#)]
32. Newman, K.M.; Schwartz, C.S.; Liu, Z.; Shao, H.; Huang, X.-Y. Evaluating forecast impact of assimilating microwave humidity sounder (MHS) radiances with a regional ensemble Kalman filter data assimilation system. *Weather Forecast.* **2015**, *30*, 964–983. [[CrossRef](#)]
33. Schwartz, C.S.; Liu, Z.; Chen, Y.; Huang, X.-Y. Impact of assimilating microwave radiances with a limited-area ensemble data assimilation system on forecasts of Typhoon Morakot. *Weather Forecast.* **2012**, *27*, 424–437. [[CrossRef](#)]
34. Lawrence, H.; Bormann, N.; Sandu, I.; Day, J.; Farnan, J.; Bauer, P. Use and impact of Arctic observations in the ECMWF Numerical Weather Prediction system. *Q. J. R. Meteorol. Soc.* **2019**, *145*, 3432–3454. [[CrossRef](#)]
35. Lu, Q.; Lawrence, H.; Bormann, N.; English, S.; Lean, K.; Atkinson, N.; Bell, W.; Carminati, F. *An Evaluation of FY-3C Satellite Data Quality at ECMWF and the Met Office*; European Centre for Medium-Range Weather Forecasts: Reading, UK, 2015; Volume 767.
36. Lawrence, H.; Bormann, N.; Geer, A.J.; Lu, Q.; English, S.J. Evaluation and assimilation of the microwave sounder MWHS-2 onboard FY-3C in the ECMWF numerical weather prediction system. *IEEE Trans. Geosci. Remote Sens.* **2018**, *56*, 3333–3349. [[CrossRef](#)]
37. Carminati, F.; Candy, B.; Bell, W.; Atkinson, N. Assessment and assimilation of FY-3 humidity sounders and imager in the UK Met Office global model. *Adv. Atmos. Sci.* **2018**, *35*, 942–954. [[CrossRef](#)]
38. Xian, Z.; Chen, K.; Zhu, J. All-sky assimilation of the MWHS-2 observations and evaluation the impacts on the analyses and forecasts of binary typhoons. *J. Geophys. Res.* **2019**, *124*, 6359–6378. [[CrossRef](#)]
39. Li, Y.; Chen, K.; Xian, Z. Evaluation of All-Sky Assimilation of FY-3C/MWHS-2 on Mei-yu Precipitation Forecasts over the Yangtze-Huaihe River Basin. *Adv. Atmos. Sci.* **2021**, *38*, 1397–1414. [[CrossRef](#)]
40. Chen, K.; Fan, J.; Xian, Z. Assimilation of MWHS-2/FY-3C 183 GHz Channels Using a Dynamic Emissivity Retrieval and Its Impacts on Precipitation Forecasts: A Southwest Vortex Case. *Adv. Meteorol.* **2021**, *2021*, 6427620. [[CrossRef](#)]
41. Carminati, F.; Atkinson, N.; Candy, B.; Lu, Q. Insights into the microwave instruments onboard the Fengyun 3D satellite: Data quality and assimilation in the Met Office NWP system. *Adv. Atmos. Sci.* **2021**, *38*, 1379–1396. [[CrossRef](#)]
42. Xie, Y.; Mao, L.; Chen, M.; Shi, J.; Fan, S.; Liu, R. Evaluation and Assimilation of FY-3C/D MWHS-2 Radiances in the RMAPS-ST. *Remote Sens.* **2022**, *14*, 275. [[CrossRef](#)]
43. Duncan, D.I.; Lawrence, H.; Bormann, N. Assessment of the FY-3D Microwave Instruments at ECMWF. Available online: <https://cimss.ssec.wisc.edu/itwg/itsc/itsc22/posters/12p.04.duncan.pdf> (accessed on 20 January 2023).
44. Bormann, N.; Duncan, D.; English, S.; Healy, S.; Lonitz, K.; Chen, K.; Lawrence, H.; Lu, Q. Growing Operational Use of FY-3 Data in the ECMWF System. *Adv. Atmos. Sci.* **2021**, *38*, 1285–1298. [[CrossRef](#)]
45. Michele, S.D.; Bauer, P. Passive microwave radiometer channel selection based on cloud and precipitation information content. *Q. J. R. Meteorol. Soc. A J. Atmos. Sci. Appl. Meteorol. Phys. Oceanogr.* **2006**, *132*, 1299–1323. [[CrossRef](#)]
46. Barker, D.M.; Huang, W.; Guo, Y.-R.; Bourgeois, A.; Xiao, Q. A three-dimensional variational data assimilation system for MM5: Implementation and initial results. *Mon. Weather Rev.* **2004**, *132*, 897–914. [[CrossRef](#)]
47. Parrish, D.F.; Derber, J.C. The National Meteorological Center's spectral statistical-interpolation analysis system. *Mon. Weather Rev.* **1992**, *120*, 1747–1763. [[CrossRef](#)]
48. Aires, F.; Prigent, C.; Bernardo, F.; Jiménez, C.; Saunders, R.; Brunel, P. A Tool to Estimate Land-Surface Emissivities at Microwave frequencies (TELSEM) for use in numerical weather prediction. *Q. J. R. Meteorol. Soc.* **2011**, *137*, 690–699. [[CrossRef](#)]
49. Karbou, F.; Gérard, E.; Rabier, F. Global 4DVAR assimilation and forecast experiments using AMSU observations over land. Part I: Impacts of various land surface emissivity parameterizations. *Weather Forecast.* **2010**, *25*, 5–19. [[CrossRef](#)]
50. Chen, K.; Bormann, N.; English, S.; Zhu, J. Assimilation of Feng-Yun-3B satellite microwave humidity sounder data over land. *Adv. Atmos. Sci.* **2018**, *35*, 268–275. [[CrossRef](#)]
51. Baordo, F.; Geer, A. Assimilation of SSMIS humidity-sounding channels in all-sky conditions over land using a dynamic emissivity retrieval. *Q. J. R. Meteorol. Soc.* **2016**, *142*, 2854–2866. [[CrossRef](#)]
52. Geer, A.J.; Bauer, P.; Lopez, P. Direct 4D-Var assimilation of all-sky radiances. Part II: Assessment. *Q. J. R. Meteorol. Soc.* **2010**, *136*, 1886–1905. [[CrossRef](#)]

53. Baordo, F.; Geer, A.; English, S. *SSMIS Radiances over Land in the All-SKY Framework: One Year Report*; European Centre for Medium-Range Weather Forecasts: Reading, UK, 2012.
54. Lin, Y.-L.; Farley, R.D.; Orville, H.D. Bulk parameterization of the snow field in a cloud model. *J. Appl. Meteor. Climatol.* **1983**, *22*, 1065–1092. [[CrossRef](#)]
55. Kain, J.S. The Kain–Fritsch convective parameterization: An update. *J. Appl. Meteorol.* **2004**, *43*, 170–181. [[CrossRef](#)]
56. Mlawer, E.J.; Taubman, S.J.; Brown, P.D.; Iacono, M.J.; Clough, S.A. Radiative transfer for inhomogeneous atmospheres: RRTM, a validated correlated-k model for the longwave. *J. Geophys. Res.* **1997**, *102*, 16663–16682. [[CrossRef](#)]
57. Dudhia, J. Numerical study of convection observed during the winter monsoon experiment using a mesoscale two-dimensional model. *J. Atmos. Sci.* **1989**, *46*, 3077–3107. [[CrossRef](#)]
58. Jiménez, P.A.; Dudhia, J.; González-Rouco, J.F.; Navarro, J.; Montávez, J.P.; García-Bustamante, E. A revised scheme for the WRF surface layer formulation. *Mon. Weather Rev.* **2012**, *140*, 898–918. [[CrossRef](#)]
59. Niu, G.Y.; Yang, Z.L.; Mitchell, K.E.; Chen, F.; Ek, M.B.; Barlage, M.; Kumar, A.; Manning, K.; Niyogi, D.; Rosero, E. The community Noah land surface model with multiparameterization options (Noah-MP): 1. Model description and evaluation with local-scale measurements. *J. Geophys. Res.* **2011**, *116*, D12109. [[CrossRef](#)]
60. Dee, D.P. Variational bias correction of radiance data in the ECMWF system. In Proceedings of the ECMWF Workshop on Assimilation of High Spectral Resolution Sounders in NWP, Reading, UK, 28 June–1 July 2004; pp. 97–112.
61. Roebber, P.J. Visualizing multiple measures of forecast quality. *Weather Forecast.* **2009**, *24*, 601–608. [[CrossRef](#)]
62. Geer, A.J.; Bormann, N.; English, S. *All-Sky Assimilation of Microwave Humidity Sounders*; ECMWF Technical Memoranda 741; European Centre for Medium-Range Weather Forecasts: Reading, UK, 2014.

**Disclaimer/Publisher’s Note:** The statements, opinions and data contained in all publications are solely those of the individual author(s) and contributor(s) and not of MDPI and/or the editor(s). MDPI and/or the editor(s) disclaim responsibility for any injury to people or property resulting from any ideas, methods, instructions or products referred to in the content.